Investigating the influence of radio-faint AGN activity on the infrared-radio correlation of massive galaxies

Giorgia Peluso^{1,*} \odot ¹, Ivan Delvecchio^{**} \odot ¹, Jack Radcliffe \odot ^{2,3}, Emanuele Daddi \odot ⁴, Roger Deane \odot ^{3,5}, Matt Jarvis \odot ⁶, Giovanni Zamorani \odot ¹ Isabella Prandoni \odot ⁷, Myriam Gitti \odot ^{7,8}, Cristiana Spingola \odot ⁷, Francesco Ubertosi \odot ^{7,8}, Mark Sargent \odot ⁹, Vernesa Smolčić \odot ¹⁰, Wuji Wang \odot ¹¹, Jacinta Delhaize \odot ¹², Shuowen Jin \odot ^{13,14}, and Adam Deller \odot ¹⁵

- ¹ INAF Osservatorio di Astrofisica e Scienza dello Spazio di Bologna, via Gobetti 93/3, I-40129, Bologna, Italy
- ² Jodrell Bank Centre for Astrophysics, University of Manchester, Oxford Road, Manchester M13 9PL, UK
- ³ Department of Physics, University of Pretoria, Lynnwood Rd, Hatfield, Pretoria, 0002, South Africa
- ⁴ CEA, Universitè Paris-Saclay, Université Paris Citè, CNRS, AIM, 91191, Gif-sur-Yvette, France
- ⁵ University of the Witwatersrand, Enoch Sontonga Ave, Johannesburg, South Africa
- ⁶ University of Birmingham, Birmingham B15 2TT, United Kingdom
- ⁷ INAF Istituto di Radioastronomia, via Gobetti 101, I–40129, Bologna, Italy
- ⁸ Dipartimento di Fisica e Astronomia (DIFA), Università di Bologna, via Gobetti 93/2, I-40129 Bologna, Italy
- ⁹ Institute of Physics, Laboratory of Astrophysics, École Polytechnique Fédérale de Lausanne (EPFL), 1290 Sauverny, Switzerland
- Department of Physics, University of Zagreb, Bijenička cesta 32, Zagreb, Croatia
- ¹¹ Caltech/IPAC, 1200 E. California Blvd. Pasadena, CA 91125, USA
- ¹² University of Western Australia, 35 Stirling Hwy, Crawley WA 6009, Australia
- ¹³ Cosmic Dawn Center (DAWN), Denmark
- ¹⁴ DTU Space, Technical University of Denmark, Elektrovej 327, 2800 Kgs. Lyngby, Denmark
- Swinburne University of Technology, John Street, Hawthorn, Victoria, Australia, 3122

2025

ABSTRACT

Context. It is well-known that star-forming galaxies (SFGs) exhibit a tight correlation between their radio and infrared emissions, commonly referred to as the infrared-radio correlation (IRRC). Recent empirical studies have reported a dependence of the IRRC on the galaxy stellar mass, in which more massive galaxies tend to show lower infrared-to-radio ratios (q_{IR}) with respect to less massive galaxies. One possible, yet unexplored, explanation is a residual contamination of the radio emission from active galactic nuclei (AGN), not captured through "radio-excess" diagnostics.

Aims. To investigate this hypothesis, we aim to statistically quantify the contribution of AGN emission to the radio luminosities of SFGs located within the scatter of the IRRC.

Methods. Our VLBA program "AGN-sCAN" has targeted 500 galaxies that follow the q_{IR} distribution of the IRRC, i.e., with no prior evidence for radio-excess AGN emission based on low-resolution (\sim arcsec) VLA radio imaging. Our VLBA 1.4 GHz observations reach a 5σ sensitivity limit of 25μ Jy/beam, corresponding to a radio brightness temperature of $T_b \sim 10^5$ K. This classification serves as a robust AGN diagnostic, regardless of the host galaxy's star formation rate.

Results. We detect four VLBA sources in the deepest regions, which are also the faintest VLBI-detected AGN in SFGs to date. The effective AGN detection rate is 9%, when considering a control sample matched in mass and sensitivity, which is in good agreement with the extrapolation of previous radio AGN number counts. Despite the non-negligible AGN flux contamination (~30%) in our individual VLBA detections, we find that the peak of the q_{IR} distribution is completely unaffected by this correction. Although we cannot rule out a high incidence of radio-silent AGN at (sub) μ Jy levels among the VLBA non-detections, we derive a conservative upper limit of < 0.1 dex to their cumulative impact on the q_{IR} distribution. We conclude that residual AGN contamination from non-radio-excess AGN is unlikely to be the primary driver of the M_{\star} - dependent IRRC.

1. Introduction

Star-forming galaxies show a positive relation between total infrared (L_{IR}, rest-frame 8-1000 μm) and monochromatic radio luminosity (e.g. at 1.4 GHz; L_{1.4}), which keeps remarkably tight ($\sigma \sim 0.26$ dex; e.g. Bell 2003) and linear for over three orders of magnitude in both $L_{\rm IR}$ and L_{1.4GHz} (e.g., Helou & Rowan-Robinson 1985; Condon 1992, even though a mild non-linearity was also found in low-z galaxies, e.g. at z < 0.2 Molnár et al. 2021).

* Email: giorgia.peluso@inaf.it** Email: ivan.delvecchio@inaf.it

This is generally known as the "infrared-radio correlation" (IRRC). The origin of the IRRC arises from the relationship between radio luminosity and (obscured) star formation rate (SFR). Broadly speaking, the IR emission arises from the light of massive OB stars, which is absorbed and re-emitted by dust (Madau & Dickinson 2014), and therefore directly traces the galaxy's SFR. On the other side, radio-continuum emission at GHz frequencies originates mainly from synchrotron processes, produced by relativistic cosmic ray electrons (CRe) accelerated by shock waves produced when massive stars (> $8M_{\odot}$) explode as supernovae, in the case of star-forming galaxies (SFG).

The logarithmic ratio between the two luminosities, labelled " q_{IR} ", is defined as:

$$q_{IR} = \log\left(\frac{L_{IR}[W]}{3.75 \times 10^{12}[Hz]}\right) - \log(L_{1.4GHz}[W/Hz])$$
 (1)

where 3.75×10^{12} Hz represents the central frequency over the far-infrared (e.g., 42-122 μ m) regime.

However, the nature of the cosmic evolution of the IRRC has long been debated (e.g., Harwit & Pacini 1975; Rickard & Harvey 1984; de Jong et al. 1985; Helou & Rowan-Robinson 1985; Hummel et al. 1988; Condon 1992; Garrett 2002; Appleton et al. 2004; Jarvis et al. 2010; Sargent et al. 2010; Ivison et al. 2010a,b; Bourne et al. 2011; Magnelli et al. 2015; Delhaize et al. 2017; Gürkan et al. 2018; Molnár et al. 2018; Algera et al. 2020; Basu et al. 2015; Rivera et al. 2017).

Several studies (Magnelli et al. 2015; Rivera et al. 2017; Delhaize et al. 2017) observed a dependence of the IRRC on the redshift, in the form of $q_{IR} \propto (1+z)^{\delta}$ with $-0.1 < \delta < -0.2$. Other works (Gürkan et al. 2018; Smith et al. 2021; Delvecchio et al. 2021, D21 hereafter) have recently argued that the IRRC evolves primarily with M_{\star} , with more massive galaxies showing a systematically lower q_{IR} , while the dependence on the redshift is secondary and weaker, as indeed $q_{IR} \propto (1+z)^{-0.023\pm0.008}$ at fixed stellar mass (see also, Gürkan et al. 2018; Smith et al. 2021). Among the possible physical drivers of the q_{IR} decline observed in massive star-forming galaxies, the energy loss of cosmic ray electrons (CRe) has been suggested to play a significant role (e.g. Schober et al. 2023; Yoon 2024). Specifically, Yoon (2024) modelled the CRe energy-loss as a function of the gas density and redshift of the host galaxy. Their findings indicate an anticorrelation between these quantities: specifically, galaxies with higher gas densities (or, equivalently, higher stellar masses, e.g. Kennicutt 2003), experience less intense energy losses, arguably because they retain more easily their CRes. On the reverse, less massive galaxies are generally most affected by CRe's energy losees. As a consequence of these synchrotron energy losses, less massive galaxies have lower radio luminous with respect to more

One yet unexplored explanation for the M_{\star} -evolution is that a hidden and widespread contribution from radio AGN activity might be driving the decline of the q_{IR} , especially at high stellar masses ($\log(M_{\star}/M_{\odot}) \ge 10$).

One very powerful tool to assess the nature of radio emission is the brightness temperature of the emitter (T_b) , defined as:

$$T_b[K] = 1.22 \times 10^6 \times (1+z) \times \left(\frac{S_{obs}}{\mu \text{Jy}}\right) \left(\frac{v}{GHz}\right)^{-2} \left(\frac{\theta_x \cdot \theta_y}{mas^2}\right)^{-1} \quad (2)$$

where S_{obs} is the observed density flux at the frequency ν and θ^x and θ^y are the major and minor axes of the beam (Ulvestad et al. 2004).

Traditionally, high T_b measurements ($T_b \ge 10^5 \mathrm{K}$) require Very Long Baseline Interferometry (VLBI), which reach milliarcsec resolutions at GHz frequencies (e.g., Middelberg et al. 2010, 2013; Rampadarath et al. 2015; Herrera-Ruiz et al. 2017, 2018; Radcliffe et al. 2018, 2021; Njeri et al. 2023; Deane et al. 2024). Recent studies performed with the Very Long Baseline Array (VLBA) at few milli-arcsec (mas) resolution (e.g., 10 mas \sim 80 pc at z=2) have identified AGN even in galaxies whose emission is dominated by star formation at Very Large Array (VLA) scales (Herrera-Ruiz et al. 2017, 2018; Maini et al. 2017). However, these pioneering studies have been highly biased towards radio-excess AGN (i.e., showing excess radio emission relative to that expected from pure star formation; V. et al. 2017.

Our project 'AGN-sCAN' extends this type of analysis by targeting with the VLBA a representative sample of SFGs without strong VLA radio-excess, down to a sensitivity reaching as deep as $\sigma \approx 5 \,\mu$ Jy/beam at 1.4 GHz, at high angular resolution (average beam size: 26×7 mas²). From Eq. 2, the T_b limit at >5 σ for an unresolved source at z=0.5 is $T_b \geq 10^5$ K 1 . Compact radio cores (\sim mas scales) characterized by such T_b would unambiguously arise from an AGN (Condon 1992; Radcliffe et al. 2018; Morabito et al. 2022).

Section 2 describes the main physical properties of the radio targets composing the sample used in this work; Section 3 summarizes the AGN-sCAN observational strategy and data products, of which a complete and detailed description will be presented by Delvecchio et al. in prep. (D25 hereafter); Section 4 summarizes our main result: the contribution of AGN emission to the nuclear emission of SFGs, classified through the IRRC, is negligible.

We adopt a Chabrier et al. (2003) initial mass function in the mass range 0.1-100 M_{\odot} . We assume a standard ΛCDM cosmology with Ω_m =0.3, Ω_{Λ} = 0.7 and H_0 = 70 km s⁻¹ Mpc⁻¹. We define the radio spectral index α with the following convention: $S_{\nu} \propto \nu^{-\alpha}$, where S_{ν} is the flux density at a frequency ν .

2. Sample selection and physical properties

This VLBA program (ID: VLBA/20B-140, PI: Delvecchio) has targeted 500 massive ($M_{\star} \geq 10^{10}~M_{\odot}$) star-forming galaxies in the Cosmic Evolution Survey (COSMOS, (Scoville et al. 2007)), which is an equatorial 2 deg² field observed with all major space-and ground-based telescopes². We refer to D25 for the detailed description of the survey.

The parent galaxy sample was retrieved from the COSMOS-Web survey (Casey et al. 2023), containing deep imaging in four JWST/NIRCam filters (F115W, F150W, F277W, F444W) over 0.54 deg² (Franco et al. 2025), and with JWST/MIRI 7.7 μ m over 0.2 deg² (Harish et al. 2025). Given that our VLBA pointing lies within the COSMOS-Web NIRCam footprint, we update all redshifts and counterpart properties from the latest COSMOS-Web photometric catalogue (Shuntov et al. 2025), which extends in wavelength out to *Spitzer*-IRAC bands. Photometric redshifts are in very good agreement with spectroscopic measurements (i.e. median absolute deviation σ_{MAD} ~0.012 at m_{F444W} <28; see Khostovan et al. 2025). We adopt the spectroscopic measurement if available and reliable (>95% confidence level) based on the compilation by Khostovan et al. (2025).

In order to retrieve a q_{IR} measurement for each target, we require our galaxies to have been detected ($\geq 5\sigma$) at both infrared (IR) and radio frequencies. The combined IR dataset comes from de-blended far-infrared/sub-mm data from *Herschel* (100–500 μ m), SCUBA2 (450, 850 μ m), AzTEC-1.1 mm, MAMBO-1.2 mm (Jin et al. 2018), and ALMA from the recent A³COSMOS survey (Liu et al. 2019; Adscheid et al. 2024), whenever available. For each source, the total IR luminosity (8-1000 μ m, L_{IR}) is obtained via spectral energy distribution (SED) fitting, and corrected for potential IR-AGN emission (Jin et al. 2018). Radio counterparts are jointly taken from MIGHTEE

¹ This value is calculated for the elongated VLBA beam in the COS-MOS field (0.027"x0.007", at Dec=2deg), hence this limit differs, at fixed depth, from that of other VLBA surveys at northern declinations (e.g.GOODS-N Deane et al. 2024).

² An exhaustive overview of the COSMOS field is available at: http://cosmos.astro.caltech.edu/ and all the relevant datasets for this study are detailed in D25.

1.28 GHz (6" resolution, Jarvis et al. 2016; Heywood et al. 2022), VLA 1.4 GHz (1.5" resolution, Schinnerer et al. 2010) and VLA 3GHz (0.75" resolution, V. et al. 2017) imaging. The rest-frame 1.4 GHz luminosity $(L_{1.4})$ is derived from the radio dataset with the highest available S/N, and K-corrected to restframe 1.4 GHz by assuming a power law spectrum with spectral index α between 3 GHz and 1.28/1.4 GHz, or assuming α =0.75 if not jointly detected. To match the spatial resolutions between the 3 GHz and 1.4 GHz images, we downgraded the 3 GHz map by convolving it with a Gaussian kernel of 1.5" FWHM (similarly to, e.g., Gim et al. 2019). We refrain from using a larger FWHM (i.e. for 1.28 GHz counterparts from MeerKAT), as Delhaize et al. (2017) showed that the flux increase above 1.5" is typically negligible. The new 3 GHz fluxes at 1.5" resolution are higher by 6%, on average, compared to those of the native resolution (0.75") map. This effect induced a minimal flattening in the re-calculated spectral index for the joint 1.4-3 GHz detections (see Sec 4.4.1 in Delhaize et al. 2017, for a in-depth discussion about the influence of the radio spectral index on the IRRC).

As for the IR part, we require that the combined S/N (summed in quadrature over all *Herschel*, SCUBA2, AzTEC, and ALMA bands) is higher than 5. For the same reason, for the radio part, we require the 1.4 GHz flux to be higher than 25μ Jy, that is $5\times$ the VLBA 1.4 GHz sensitivity at the pointing center. We restrict ourselves to galaxies at z>0.5, in order to get the full galaxy size within the VLBA field of view limited by bandwidth smearing (i.e. 5.5'' diameter). We disregard all previously detected VLBA targets from Herrera-Ruiz et al. (2017; 2018) to avoid duplications.

These selection criteria naturally identify 500 massive $(M_{\star} \gtrsim 10^{10} \ M_{\odot})$ galaxies. This sample is representative of star-forming galaxies on the IRRC, as they are broadly distributed in q_{IR} around the (M_{\star},z) -dependent IRRC from Delvecchio et al. (2021) (see also Sec 4 for details).

3. Observation and data calibration

Our VLBA observations are summarized in the following, while further details will be given in D25. In each VLBA session, the full L-band bandwidth is split in 8 spectral windows of 32 MHz each, further divided in 16 spectral channels (2 MHz each) at 4sec time resolution. This setup yields a field of view limited by time (bandwidth) smearing of 10.82" (2.75"), hence larger than the typical galaxy size at z>0.5 (Yang et al. 2025). The final images of all targets, consisting of 4096×4096 pixels (at 0.001"/px scale) weight about 67 Mbyte each ³.

The pointing center was located at RA (J2000) = 10:00:36.3299 and Dec (J2000) = +02:12:58.773 and covers 30′ FWHM at 1.4 GHz. It was observed for a total of 120 hr, split in 24 epochs of 5-hr each, due to the limited visibility of COSMOS by all 10 VLBA antennas for longer tracks. Raw data were calibrated using the VLBI PIPEline (VPIPE; Radcliffe et al. 2024, Radcliffe et al., in prep., ⁴) that is designed to perform automated instrumental calibration, phase referencing, and imaging for multi-phase centre VLBI observations. All these steps have been successfully tested in former very long baseline surveys (EVN from Radcliffe et al. 2018; Radcliffe et al. 2021; VLBA from Deane et al. 2024).

In order to evaluate the significance of each VLBA source as a function of the peak S/N, we have run simulations using the Common Astronomy Software Applications (CASA, v.6.6) package. We refer the reader to D25 for more technical details on this task. Briefly, we considered the real noise map, taken from an empty sky region at the VLBA pointing centre, and inject one point-like source in the *uv*-plane, with known position and S/N. We iterated the simulation 100 times, keeping the input position fixed but varying the input S/N over the range $4.5 \le S/N \le 7.5$. Only one source was injected into each realization, in order to mitigate sidelobe effects and obtain reliable output fluxes (see D25). We then imaged each simulated dataset adopting the same setup used for real data and employing BLOBCAT Hales et al. (2012) to extract the flux and position of all blobs above a given peak S/N, in each image. While the completeness at S/N>4.5 is always observed to be higher than 90% (i.e. BLOBCAT finds the one input source in >90% of runs), the fraction of spurious blobs is a strong function of S/N. In particular, we defined the "spuriousness" (p_{spur}) as:

$$p_{spur} = 1 - \frac{N_{inp}}{N_{out}} \tag{3}$$

where N_{inp} is the number of 'real' (input) blobs and N_{out} is the number of the (output) detected blobs. We count the output blobs within a radius of $\pm 0.2''$ from the input (real) source, similarly to what we do for real detections (see Sect.3.1). We find that the spuriousness is higher than 50% at S/N <5, while it decreases to $\approx 15\%$ at S/N ≈ 5.5 , and exponentially drops below 2% at S/N ≈ 6 . If counting all random blobs over the full image (4"×4"), the spuriousness at fixed S/N increases proportionally to the searching area, except at S/N ≈ 6 where it drops to below 2% as found in the central area.

3.1. Final sample of VLBA detections

Following Herrera-Ruiz et al. (2017) (HR2017, hereafter), we obtain the total fluxes from BLOBCAT (Hales et al. 2012) by integrating the blobs with $S/N \ge 5.5$ that are found within $\pm 0.2''$ that is ±1 VLA 3 GHz pixel from the prior VLA counterpart position (V. et al. 2017), which sets our maximum VLBA-VLA separation - in HR2017 it was ± 0.4 ", i.e. ± 1 VLA 1.4 GHz pixel (Schinnerer et al. 2010). For consistency, our chosen size of ± 0.2" is also the circular region inside which we forced the cleaning in order to maximize the S/N (D25). Based on the above criteria, we identify 4 VLBA detections associated with AGN activity, with their main properties listed in Table 1. We also show them in Figure 1, where the presence of a compact radio core is evident (e.g., purple contours). The average VLBA rms of these four detections is 6μ Jy/beam. Interestingly, these sources are the faintest AGN ever detected with VLBI techniques in SFGs. If pushing our detections threshold at lower S/N, in particular at 5.0 < S/N < 5.5, we would identify two additional source candidates, but their high spuriousness (~40% at their average $S/N\sim5.2$) does not allow us to claim them as secure detections.

We note in Fig.1 that the VLBA (iso-surface brightness) contours appear more complex than the elongated synthesized beam. This is because 3 out of 4 detections (all but '498') are marginally resolved (along the beam minor axis), according to BLOBCAT (Hales et al. 2012). However, given the low S/N of these detections, the limited *uv*-coverage and the lack of a-priori information on the source morphology, the imaging and deconvolution process becomes highly uncertain (e.g. tay 1999). In such conditions, the final restored contours can be a complex

³ The images are publicly available at: https://github.com/idelvecchio/AGN-sCAN_catalogue

⁴ https://github.com/jradcliffe5/VLBI_pipeline

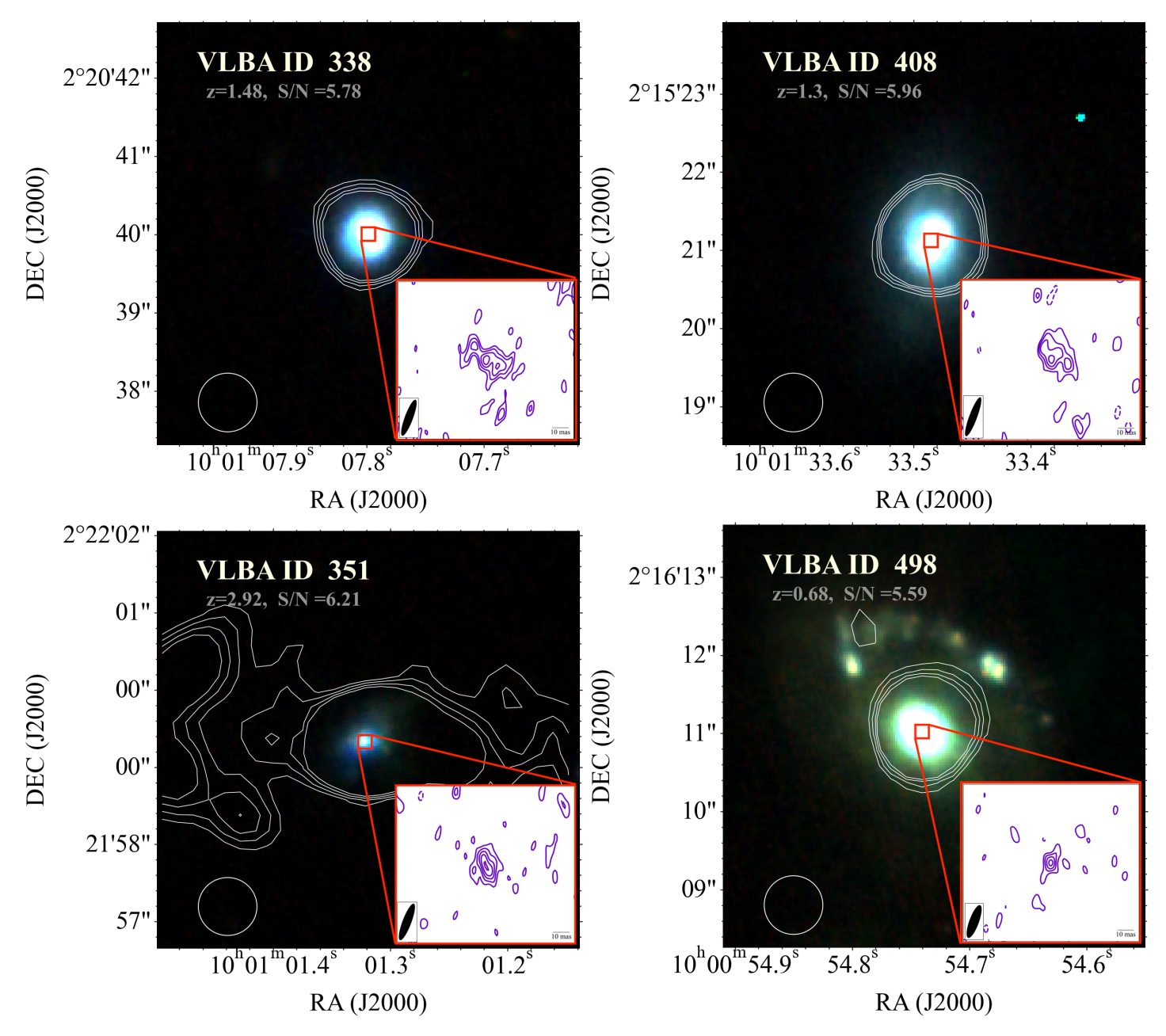


Fig. 1. RGB images of the targets VLBA ID '338' (top left), '351' (top right), '408' (bottom left), and '498' (bottom right). These are obtained by combining the F150W, F277W, and F444W JWST/NIRCam filters (Franco et al. 2025) covering a 5" \times 5" field of view. The NIRCam pixel scale is 30 mas. The white contours are the VLA 3 GHz levels (V. et al. 2017) at 3, 4, 5, and 6 times the rms (2.3 μ Jy/beam, the VLA beamsize is 0.75" as shown by the white circle in the bottom left). In the zoom-in red panels, the purple contours are the levels at 2, 3, 4, 5, and 6 times the image rms detected by the VLBA, which come from a 0.2" \times 0.2" field of view, also outlined by the red square at the centers of the galaxies. The dotted purple contour also shows the -3 rms level. The VLBA beam size for each detection is: 26 \times 5 mas² ('338'), 26 \times 5 mas² ('351'), 28 \times 5 mas² ('408'), and 23 \times 6 mas² ('498'), with a similar position angle PA \sim 162°.

blend of different spatial components and are not expected to strictly follow the shape of the clean beam, hence some contours of faint sources would appear rounder and/or smaller than the synthesized beam. This is a known issue in deep VLBI imaging and has been observed in other VLBI surveys (e.g., Radcliffe et al. 2018). Because the 3 resolved detections display non-Gaussian morphologies, as recommended in Hales et al. (2012) we do take total VLBA fluxes (e,g, S_{VLBA} in Table 1) from the corresponding observed integrated values, but skipping the Gaussian volume correction. For the only unresolved detection ('498'), instead, we set the total flux equal to the peak flux.

In order to make a fair comparison between our VLBA detections and non-detections, we define two control samples of VLBA non-detections ("CS" hereafter): (i) a M_{\star} -matched CS (i.e., with log $(M_{\star}/M_{\odot}) > 10.5$; 277 objects) and a combined $[M_{\star}, rms]$ -matched CS (i.e. a subset of the first CS, with also rms < 6.7 μ Jybeam⁻¹, i.e. the highest among the 4 detections; 42 objects). Therefore, this latter CS contains the VLBA targets which were not detected within a depth-matched area, despite being evenly accessible as for the VLBA detections. Overall, the effective detection rate in our sample is 9% (i.e. 4/46), which is broadly consistent with the AGN duty cycle in massive starforming galaxies (Delvecchio et al. 2022; Wang et al. 2022). We

ID _{VLBA}	RA [deg]	DEC [deg]	z	$\log(M_{\star}/M_{\odot})$	rms _{VLBA} [μJy/beam]	$S_{ m VLBA} \ [\mu m Jy]$	$\log L_{ m VLBA} \ [m W/Hz]$	$\log L_{ m VLA} \ [m W/Hz]$	$\log(L_{\rm IR}/{ m L}_{\odot})$	<i>q</i> _{IR}
338	150.28249	2.34445	1.48	10.85±0.04	5.6	50.2 ±12.9	23.77±0.13	24.19±0.02	12.14±0.04	1.95±0.04
351	150.25549	2.36649	2.92	10.80±0.04	6.1	41.4 ±9.3	23.88±0.11	24.80±0.02	12.62±0.15	1.84±0.15
408	150.38951	2.25589	1.30	11.10±0.04	5.6	58.2 ±13.4	23.69±0.11	24.20±0.08	11.87±0.05	1.68±0.09
498	150.22804	2.26971	0.68	10.65±0.04	6.7	37.2 ±7.8	22.79±0.10	23.32±0.03	11.69±0.03	2.37±0.04

Table 1. Columns are: 1) VLBA identification number; 2) and 3) VLBA centroid coordinates; 4) spectroscopic redshifts: z = 1.48 (Kashino et al. 2019), z = 2.92 (Horowitz et al. 2022), z = 1.30 (Kartaltepe et al. 2015), z = 0.68 (van der Wel et al. 2021); 5) stellar mass in Chabrier IMF (Shuntov et al. 2025); 6) average VLBA rms (μ Jy/beam); 7) rest-frame VLBA 1.4GHz flux density in μ Jy (S_{VLBA}); 8) rest-frame VLBA 1.4GHz luminosity; 9) VLA 1.4GHz rest-frame radio luminosity; 10) total IR luminosity (rest-frame 8-1000 μ m) obtained from SED-fitting with deblended IR fluxes; 11) IR-to-radio luminosity ratio (see Equation 1).

note that matching the control sample by the lowest or the average rms of the detections would not have changed the effective detection rate.

4. The AGN corrected infrared-to-1.4 GHz radio luminosity ratio

We measured q_{IR} exploiting the total radio VLA luminosities, where both star formation and AGN activity can, in principle, contribute. Figure 2 shows these values as a function of the stellar mass of the host galaxy. Dark stars mark the 4 detections, the light blue circles indicate the M_{\star} -matched CS, while the darker blue circles represent the (M_{\star}, rms) - matched CS. The black solid line represents the dependence of the IRRC on the stellar mass for galaxies at a $\langle z \rangle \sim 1$, as indicated by the relationship described by Delvecchio et al. (2021):

$$q_{IR}(M_{\star}, z) = 2.646 \pm 0.024 \times A^{-0.023 \pm 0.008} - B \times (0.148 \pm 0.013)$$
 (4)
where $A = (1 + z)$ and $B = \log(M_{\star}/M_{\odot})$.

It is important to note that the dependence on the stellar mass is stronger than that with the redshift. To measure the $q_{IR}(M_{\star},z)$, we consider the stellar masses and redshifts presented in Sec 3. Since the $q_{IR}(M_{\star},z)$ distributions are similar between the M_{\star} -and (M_{\star},rms) - matched CS (as expected given that the observed q_{IR} does not depend on the VLBA rms), in the following we consider the $q_{IR}(M_{\star},z)$ distribution of the M_{\star} -matched CS to increase the statistics.

If we assume that the incidence of AGN is as high as in the deepest regions across the entire sky area mapped by the AGN-sCAN survey, we can then reason that the number of effective detections would have been 7 times greater than the $N_{AGN} = 4$ detected in regions with rms <6.7 μ Jy/beam. This factor of seven was determined by noting that the subset of non-detections matched on both stellar mass and rms, (M_{\star} , rms)-CS, is approximately seven times smaller than the subset matched solely by stellar mass (e.g., M_{\star} -CS).

Then, we measured the difference (Δq_{IR}) between $q_{IR}(M_{\star},z)$ and the observed q_{IR} computed using the VLA luminosities in Eq. 1. On the left panel of Fig. 3, the light purple histogram displays the distribution of Δq_{IR} for the (M_{\star} , rms)-CS, while the dark purple histogram displays the distribution of Δq_{IR} for the detections. To reproduce the expected IRRC for pure SFG, we build up the so-called 'mirror distribution' (orange dashed histogram). This is obtained by mirroring the right side of the real distributions, assumed to be purely originating from SF processes, onto the left side. The errors associated with the counts

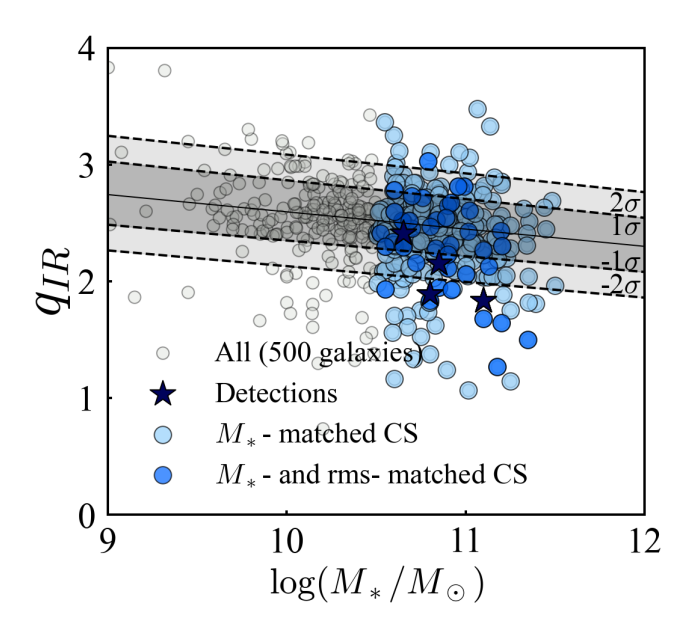


Fig. 2. q_{IR} distribution as a function of host galaxy stellar mass for all the 500 targets (grey points), the 4 VLBA-detected AGN (blue stars) and the 277 non-detections part of the M_{\star} -matched sample (light blue points). The q_{IR} of the detections account for the AGN emission detected by the VLBA (e.g., $q_{IR,corr}$). The darker blue points are the 42 non-detections observed at sensitivities equal to or lower than the sensitivity of the detections, thus constituting the (M*, rms)- matched CS. The black line is the q_{IR} versus $\log M_{\star}/M_{\odot}$ relation from Delvecchio et al. (2021) at $< z > \sim 1$, and the shaded areas spans the scatter of the IRRC at $M_{\star} > 10^{10.5} M_{\odot}$ from Delvecchio et al. (2021), of around \pm 0.22 dex and \pm 0.44 dex.

of the mirror distributions (orange shaded area) are calculated with a bootstrap, by extracting 1000 values from a Gaussian distribution centered on the observed number counts (N), in each bin, with a standard deviation of \sqrt{N} . We observe that the mirror distribution peaks around 0 in both panels. This allows us to visually assess how much the observed distribution deviates from a perfect Gaussian. In the right-hand panel of Fig. 3, we instead plot the distributions of the difference between $q_{IR}(M_{\star},z)$ and the corrected $q_{IR}(q_{IR,corr})$, after subtracting the AGN emission observed with the VLBA. In this case, $\Delta q_{IR,corr}$ equals $\log[(L_{VLA})/(L_{VLA}-L_{VLBA})]$, which is > 0 by definition.

The first thing to note is that the median values of the real distributions remain unchanged before and after the correction for the AGN contribution to the radio luminosities. Both before and after the correction, we estimate $\langle \Delta_{qIR} \rangle = 0.0^{+0.03}_{-0.02}$ dex. The errors on the median are calculated as the 16th and 84th per-

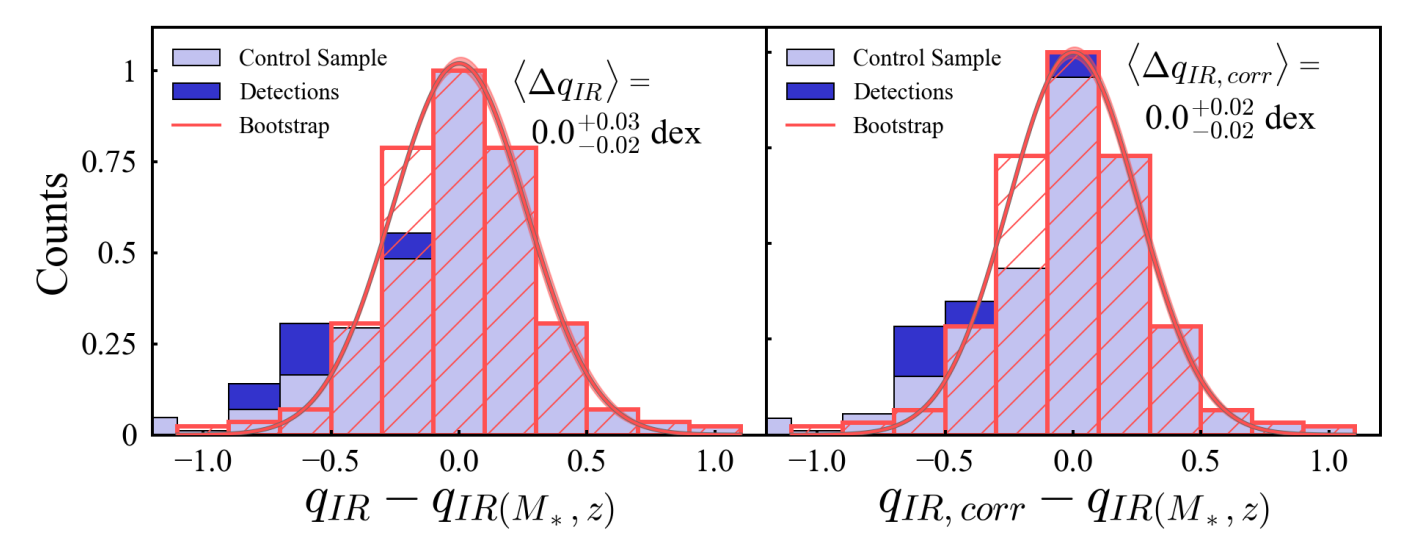


Fig. 3. Normalized distributions of the difference between the observed q_{IR} and the one expected from Eq. 4 (Delvecchio et al. 2021) based on the stellar mass and the redshift of the host galaxy, q_{IR} (M_{\star} ,z). The light purple histogram represents the distribution of the (M_{\star} ,z)-CS. The stacked dark purple histogram (i.e. dark purple histogram on top of the light purple one)

represents the detections, and the hatched orange histogram is the so-called mirror distribution, interpreted as the intrinsic q_{IR} distribution of SFGs. The bootstrapped median values of the mirror distribution were fitted with a Gaussian (red curve; see Sec. 4 for further details). Left panel: q_{IR} is computed using the VLA luminosity coming from both star formation and AGN activity. Right panel: $q_{IR,corr}$ is the ratio measured after subtracting the AGN radio luminosity detected by the VLBA from the total radio VLA emission.

centiles of the distribution, divided by the square root of the total counts. However, it was expected that the AGN contribution would have minimal impact on the scatter within the IRRC for these galaxies, due to the low fraction of detections.

Nevertheless, it is interesting to note that on an individual source basis, the AGN fluxes substantially influence q_{IR} , since the average difference between q_{IR} and $q_{IR,corr}$ for the detections is about 0.14 dex (e.g. 30%), which is not negligible.

To further explore the potential role of radio variability, we examined the list of variable 1.5 GHz sources identified in the CHILES VERDES survey (Sarbadhicary et al. 2021). The survey provides 1-2 GHz continuum VLA data obtained between 2013 and 2019 in a 0.44 deg^2 area of the COSMOS field for 750 previously detected at VLA-1.4GHz. Moderate variability (10-30% flux density variation) was observed in 18 sources, and low-variability (2-10% flux density variation) in 40 sources, for a total of 58/750 (6%) variable targets. Only one of those variable sources is in common with our VLBA 1.4 GHz targets (even though it is not a VLBA detection) and exhibits low VLA variability (±5%). Moreover, based on the comparison between VLBA-1.4GHz (Herrera-Ruiz et al. 2017) and VLA-1.4GHz (Schinnerer et al. 2010) fluxes taken at different epochs (2012 vs 2007, respectively), Herrera-Ruiz et al. (2017) found 13/468 (~3%) VLBA detections with VLBA flux higher than the total VLA flux (at above $>\pm 1\sigma$ uncertainty), which the authors interpreted as possible sign of variability. However, those 13 sources all have $S_{vlba}>200 \mu Jy$, making them among the brightest of their sample. Hence, we expect a negligible fraction of radio-variable sources among our even fainter targets.

Then, we also find that the real distribution exhibits a deviation from the Gaussianity (e.g., when compared to the mirror distribution) on the left side, in both panels. However, this is minimal, as indeed a K-S test could not reject the hypothesis that these two distributions come from the same parent sample (with a p-value of 0.997).

Finally, we note that the mirror distributions are basically un-

changed even after correcting the q_{IR} of the detections. Besides the peak, also their standard deviations are fully consistent (from $\sigma=\pm0.44$ dex to $\sigma=\pm0.45$ dex). Overall, these results highlight that VLBA AGN contamination, despite being non-negligible for individual detections, does not impact at all the peak position (and the overall shape) of the original q_{IR} distribution.

For completeness, in Appendix A, we correct the values of q_{IR} for the dependence on redshift, and we verified that also in that case the distribution of the *z*-corrected q_{IR} distribution remains unchanged before and after the AGN correction.

5. Source counts

Following a similar approach as in Deane et al. (2024) and Herrera-Ruiz et al. (2018), we compute the differential source counts, dN/dS_{ν} , as a function of source 1.4 GHz flux density, S_{ν} , using the expression:

$$\frac{dN}{dS} = \frac{N}{\Omega \Delta S} \tag{5}$$

where N is the number of sources in a flux density bin, Ω is the area over which a source with flux density equal to the mean flux density of the bin could be detected, and Δ S is the width of the flux density bin.

Figure 4 displays the 1.4 GHz source count of the VLBA-detected AGN presented in this work (red star). For comparison, we also show the differential source counts derived by Herrera-Ruiz et al. (2018) using the VLBA COSMOS survey (as black dots), the derived source counts for the VLBA CANDELS GOODS-North Survey from Deane et al. (2024) (as red circles) and the VLA 3 GHz source counts split into SF and AGN subpopulations from Novak et al. (2018). The Novak et al. (2018) curves are obtained by statistically separating SFGs and radio AGN based on the "radio-excess" criterion (Delvecchio et al.

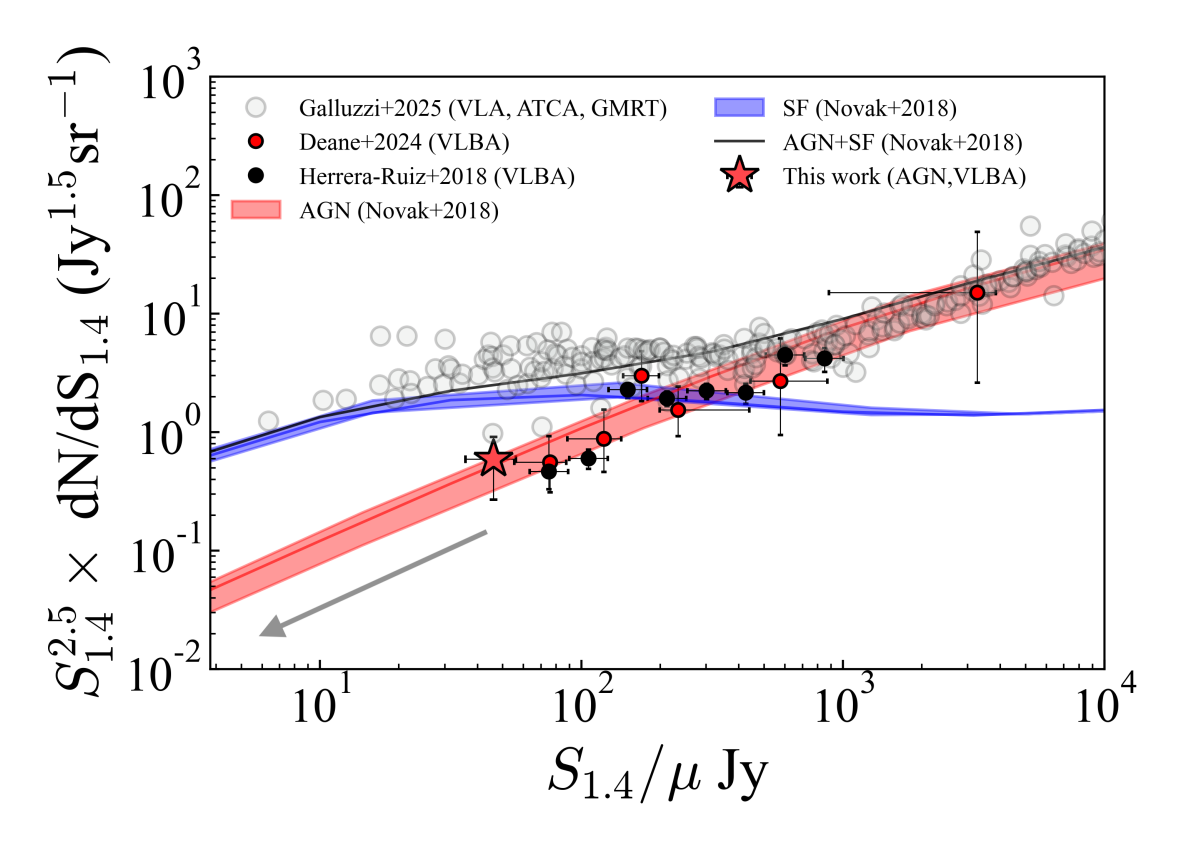


Fig. 4. Euclidean normalized radio source number counts obtained by fitting, with the Markov chain Monte Carlo algorithm, the total radio Luminosity Function (LF) from Novak et al. (2018) using different evolving analytical LFs for AGN hosts (red line) and SF galaxies (blue line). The shaded areas encompass the 3σ errors from the χ^2 fits performed on individual populations (see Novak et al. 2018, for further details). Grey circles are the number counts from Galluzzi et al. (2025) obtained from a compilation of radio observations with different instruments (e.g. VLA 1-3 GHz, ATCA, GMRT, LOFAR, MeerKAT etc.), without any distinction between AGN or SF. Red and black circles show the number counts from the VLBA CANDELS GOODS-North Survey (Deane et al. 2024) and VLBA 1.4 GHz COSMOS (Herrera-Ruiz et al. 2018) in case of radio emission from AGN activity. The red star is the number count of the detections from the AGN-sCAN survey presented in this work. The grey arrow point towards the regime below our sensitivity limit, from which the number counts extrapolated from the red curve of Novak et al. (2018) of the 42 brightest AGN were extracted, in order to constrain upper limits on our results (see text in Sec. 6.1 for further details).

2017), using data from the VLA-COSMOS 3 GHz Large Project (V. et al. 2017). Our results are perfectly consistent with these previous works, as indeed the VLBA source counts at $S_{1.4GHz} = 37-58~\mu$ Jy follow the red curve in Novak et al. (2018), which is representative of the AGN population. At these fluxes, the AGN number counts are ~5× lower than those of the total radio source population. This corroborates that the average AGN fraction of ~20% among sources within this flux regime, while ~80% of the sources are star-forming galaxies.

Our measurement in Fig. 4 (red starred symbol) is the faintest source count measurement ever obtained from VLBI studies, and aligns well with previous (low-resolution) extrapolations of AGN number counts (red solid line). In this context, Whittam et al. (2017) hinted at a possible flattening of the AGN number counts towards faint flux densities, meaning that compact, flat-spectrum radio cores are increasingly dominant in these regimes. Although we do not have enough statistics to robustly test this hypothesis, we remark that the excess of flat-spectrum radio cores could indicate the presence of younger radio jets, short duty cycles, weak jet collimation, or slower jet speeds (see Deane et al. 2024, for an in-depth discussion).

6. Discussion

6.1. Cumulative Distribution of AGN in the faintest regime

Our 5.5σ sensitivity limit enabled us to detect AGN activity with flux densities down to $< S_{1.4} > = 37-58 \mu Jy$.

Of course, we cannot rule out a widespread contribution of AGN at even fainter fluxes. Unveiling those ultra-faint AGN is, however, very challenging. VLBA stacking would improve our sensitivity limit, but it is not feasible due to to the lack of prior knowledge on the AGN position. The VLA peak flux position was indeed not sufficient to serve as a prior, as indeed the VLBA has over ×10 times higher spatial accuracy. Similarly, HST or JWST positions are significantly less accurate than VLBA positions, with the additional caveat that they could trace star formation, which might not be spatially coincident with AGN emission. Therefore, we attempt a statistical assessment of the AGN contamination in VLBA non-detections.

We derive a quantitative threshold of how faint the required flux limit would have to be, by conservatively assuming that our VLBA non-detections from the (M_{\star} , rms)-matched CS are the first 42 brightest AGN expected just below the faintest flux of our VLBA detections, i.e., at $S_{1.4} < 37~\mu Jy$.

To do so, we convert the Euclidean-normalized 1.4 GHz source counts into a dimensionless quantity, re-scaled to the effective sky area of the (M_{\star}, rms) -matched CS (i.e. 9.7 x 10^{-6} sr). This yields a number of expected AGN in the same area, as a

function of 1.4 GHz flux. We make sure that the relation between differential N_{AGN} and $S_{1.4}$ yields an integrated $N_{AGN} = 4$ in the range 36–58 μ Jy (i.e. matching our VLBA detections, red stars in Fig. 4). Then we extrapolate the same trend down, and below our nominal VLBA flux density limit. Finally, we compute the cumulative distribution of N_{AGN} at $S_{1.4} < 37 \mu Jy$, and we found out that 42 sources would be cumulated at a flux density of 5 μ Jy, which is then the minimum flux density reached by the ≈ 42 brightest AGN. We stress again that this is an over-conservative assumption, since it is very unlikely that our non-detections are all clustered just below the flux limit. However, at these low flux densities, the brightness temperature drops to $T_b \ll 10^5$ K (see Eq. 2). This suggests that, even if we were able to detect such faint sources with the VLBA, the origin of their emission would be ambiguous between AGN or SF. Consequently, we conclude that pushing VLBA observation to sub- μ Jy sensitivity would not be an effective strategy for revealing a residual hidden population of radio AGN. For instance, according to the ngVLA exposure time calculator ⁵, we note that Band 1 (2.3 GHz observations) would reach brightness temperatures $T_b \ge 10^5$ K (at 5σ , i.e. \approx 5 μ Jy/beam) in about 16h on-source. Hence, fainter fluxes, as expected for the bulk of our VLBA non-detections, would be detected with a lower $T_B < 10^5$ K, thus carrying an ambiguous origin despite their easy detection.

Furthermore, even in this conservative scenario in which our non-detections are the brightest AGN below our sensitivity limit, the ratio S_{VLBA}/S_{VLA} is 17% at $S_{VLA}\approx 70~\mu Jy$. S_{VLBA} is the mean flux of the 42 brightest AGN obtained from the cumulative distribution of the AGN number counts in the range $5~\mu Jy \leq S_{1.4} \leq 36~\mu Jy$, while S_{VLA} is the mean VLA 1.4 GHz flux density of the 42 non-detections. This ratio would translate into a global upper q_{IR} shift of <0.1 dex. We note that, based on the M_{\star} -dependent IRRC, q_{IR} decreases by 0.22 dex within the same M_{\star} range of the analysed sample (log $M_{\star}/M_{\odot} > 10.5$, Delvecchio et al. 2021). Therefore, given that radio AGN contamination (including VLBA detections and non-detections) counteracts this effect by < 0.1 dex, the decreasing q_{IR} with M_{\star} is not primarily explained by AGN contamination.

Among other possible mechanisms that have been proposed to explain the decline of q_{IR} at stellar masses $\log(M_\star/M_\odot) \geq 10.5$ in SFG, there is an increasing energy loss rate of highenergy CR electrons, which can be due to particularly efficient supernova-driven turbulence (Schober et al. 2023). The CR energy loss could also depend on the gas surface density and the redshift of the host galaxy, as modeled by Yoon (2024). Finally, Ponnada et al. (2025) found that in many cases "radio-excess" objects can be better understood as "IR-dimmed" objects with longer-lived radio contributions at low-z from Type-Ia supernovae and intermittent black hole accretion in weakly SFGs.

6.2. Diffuse AGN emission as a possible caveat

A potential caveat of this analysis is that the AGN flux could be underestimated because of extended emission (beyond the VLBA beam, e.g. $200\text{pc} \times 50\text{pc}$ at z=1), that is resolved out by the VLBA (e.g. Morabito et al. 2025). We first tested that the integrated fluxes remain consistent across various tapering and Briggs schemes in our images. We also note that additional AGN flux over more extended physical scales would correspond to a lower T_b , hence $T_b < 10^5$ K (see Eq. 2).

A statistical assessment of this AGN emission at intermediate scales comes from Herrera-Ruiz et al. (2017). The vast majority

of their VLBA detections (>90%) are classified as AGN based on the radio-excess observed from the VLA fluxes. Briefly, the "radio excess" is determined by the difference between the radio luminosity predicted by the IRRC at the redshift and stellar mass of the host galaxy (which traces star formation only) and the observed radio luminosity measured by VLA, which includes contributions from both star formation and AGN. Assuming that this radio-excess traces the full AGN-related flux over the entire galaxy size, the comparison between total VLBA and AGNdriven VLA flux indicates how much flux is lost on larger scales. We note (see Figure 11 in Herrera-Ruiz et al. 2017) that at fluxes $S_{1.4} < 50\mu Jy$, the VLBA flux is already > 75% of the total VLA AGN flux, hence highly compact. By extrapolating this trend towards fainter flux regimes (as for our VLBA targets), we would expect that the VLBA flux is capturing the vast majority (if not all) of the total AGN flux. Finally, the agreement between the predicted and observed number count in this work (Fig. 4) further supports the hypothesis that the VLBA effectively captures the full AGN emission from our targets.

7. Conclusions

We presented our 1.4 GHz VLBA observations carried out in the context of the AGN-sCAN survey (PI: Delvecchio), targeting a sample of 500 SFGs in COSMOS at z>0.5 located around the IRRC (see Fig. A.1). By exploiting this sample down to a limiting $T_B \gtrsim 10^5$ K, we could test whether the decrease of q_{IR} with galaxy stellar mass, as observed in Delvecchio et al. (2021), could be explained by residual radio contamination from radiofaint AGN buried in the total radio emission of massive starforming galaxies. To do so, we investigated the difference in the q_{IR} distribution before and after correcting for a VLBA AGN contribution.

To perform a fair comparison between detections and nondetections, we built up a (M_{\star} ,rms)-matched CS of 42 pure SFG, which did not show AGN emission as detected by the VLBA at 1.4 GHz and have stellar mass $\log(M*/M_{\odot}) \ge 10.5$.

Our findings can be summarized as follows:

- (a) We revealed a radio core in 4 targets placed in the deepest area. The effective AGN detection rate (rms-matched) in SFGs around the IRRC is $\sim 9\%$. By subtracting the VLBA AGN contribution at 1.4 GHz, we find that the q_{IR} distribution remains essentially unchanged. Indeed, the median and dispersion values of the distributions are entirely consistent with each other before and after applying this correction (as shown in the left and right panels of Fig. 3). Given that such AGN correction is negligible for $\log(M_{\star}/M_{\odot}) \geq 10.5$, we expect that it will be even less significant at lower stellar masses.
- (b) As shown in Fig. 4, the AGN number counts at $37-58\mu Jy$ lie well onto the extrapolation of the AGN number counts from Novak et al. (2018), and the AGN contribution amounts to 20% of the total number count of the entire radio population at these fluxes. Moreover, even in the extreme case that our VLBA non-detections were the brightest AGN just below the detection threshold, we still predict a maximum q_{IR} shift of <+0.1 dex. This upper limit is significantly smaller than the 0.22 dex decline of q_{IR} within the M_{\star} range of the VLBA detections, thus excluding the possibility that radio-AGN contamination is the primary driver of the M_{\star} -dependent q_{IR} .

Finally, we noted that pursuing deeper VLBA observations would not have been an effective strategy to unveil a residual

⁵ https://ngect.nrao.edu/

hidden population of even fainter AGN. Other potential physical mechanisms that could explain the q_{IR} decline in massive galaxies include CRe transport (Yoon 2024) and a longer-lived radio contribution from Type Ia supernovae (Ponnada et al. 2025). Nevertheless, our results highlight that the SFR-radio relation is robust against contamination from AGN activity, once the so-called "radio-excess" AGN are removed.

Acknowledgements. The authors thanks the referee for a constructive report that helped us clarify the results and implications of this work. G. P., I. D., M. G., F. U., and I. P. acknowledge funding by the European Union – NextGenerationEU, RRF M4C2 1.1, Project 2022JZJBHM: "AGN-sCAN: zooming-in on the AGN-galaxy connection since the cosmic noon" - CUP C53D23001120006. C. S. acknowledges financial support from INAF – Ricerca Fondamentale 2024 (Ob.Fu. 1.05.24.07.04), from the Italian Ministry of Foreign Affairs and International Cooperation (grant PGRZA23GR03), and by the Italian Ministry of University and Research (grant FIS-2023-01611, CUP C53C25000300001). W.W. acknowledges the grant support through JWST programs. Support for programs JWST-GO-03045 and JWST-GO-03950 were provided by NASA through a grant from the Space Telescope Science Institute, which is operated by the Association of Universities for Research in Astronomy, Inc., under NASA contract NAS 5-03127.

References

1999, 180

- Adscheid, S., Magnelli, B., Liu, D., et al. 2024, A&A, 685, A1
- Algera, H. S. B., Smail, I., Dudzevičiūtė, U., et al. 2020, The Astrophysical Journal, 903, 138
- Appleton, P. N., Fadda, D. T., Marleau, F. R., et al. 2004, The Astrophysical Journal Supplement Series, 154, 147
- Basu, A., Wadadekar, Y., Beelen, A., et al. 2015, Astrophysical Journal, 803, 51 Bell, E. F. 2003, The Astrophysical Journal, 586, 794
- Bourne, N., Dunne, L., Ivison, R. J., et al. 2011, Monthly Notices of the Royal Astronomical Society, Volume 410, Issue 2, pp. 1155-1173., 410, 1155
- Casey, C. M., Kartaltepe, J. S., Drakos, N. E., et al. 2023, The Astrophysical Journal, 954, 31
- Chabrier, G., Chabrier, & Gilles. 2003, PASP, 115, 763
- Condon, J. J. 1992, Annual Rev. Astron. Astrophys., Vol. 30, p. 575-611 (1992), 30, 575
- de Jong, T., Klein, U., Wielebinski, R., et al. 1985, A&A, 147, L6
- Deane, R. P., Radcliffe, J. F., Njeri, A., et al. 2024, Monthly Notices of the Royal Astronomical Society, Volume 529, Issue 3, pp.2428-2442, 529, 2428
- Delhaize, J., Smolcic, V., Delvecchio, I., et al. 2017, A&A, 602, A4
- Delvecchio, I., Daddi, E., Sargent, M. T., et al. 2022, Astronomy and Astrophysics, 668, A81
- Delvecchio, I., Daddi, E., Sargent, M. T., et al. 2021, Astronomy and Astrophysics, 647, A123
- Delvecchio, I., Smolčić, V., Zamorani, G., et al. 2017, Astronomy and Astrophysics, 602, A3
- Franco, M., Casey, C. M., Koekemoer, A. M., et al. 2025, arXiv, arXiv:2506.03256
- Galluzzi, V., Behiri, M., Giulietti, M., & Lapi, A. 2025, eprint arXiv:2504.00192, arXiv:2504.00192
- Garrett, M. A. 2002, A&A, 384, L19
- Gim, H. B., Yun, M. S., Owen, F. N., et al. 2019, The Astrophysical Journal, 875, $80\,$
- Gürkan, G., Hardcastle, M. J., Smith, D. J., et al. 2018, Monthly Notices of the Royal Astronomical Society, 475, 3010
- Hales, C. A., Murphy, T., Curran, J. R., et al. 2012, Monthly Notices of the Royal Astronomical Society, 425, 979
- Harish, S., Kartaltepe, J. S., Liu, D., et al. 2025, arXiv, arXiv:2506.03306 Harwit, M. & Pacini, F. 1975, Astrophysical Journal, vol. 200, Sept. 15, 1975,
- pt. 2, p. L127-L129., 200, L127
 Helou, G. & Rowan-Robinson, M. 1985, The Astrophysical Journal, 298, 7
- Herrera-Ruiz, N., Middelberg, E., Deller, A., et al. 2017, Astronomy and Astrophysics, 607, A132
 Herrera-Ruiz, N., Middelberg, E., Deller, A., et al. 2018, Astronomy and Astro-
- physics, 616, A128
- Heywood, I., Rammala, I., Camilo, F., et al. 2022, The Astrophysical Journal, 925, 165
- Horowitz, B., Lee, K.-G., Ata, M., et al. 2022, ApJS, 263, 27
- Hummel, E., Davies, R. D., Wolstencroft, R. D., et al. 1988, A&A, 199, 91
- Ivison, R. J., Alexander, D. M., Biggs, A. D., et al. 2010a, Monthly Notices of the Royal Astronomical Society, 402, 245

- Ivison, R. J., Magnelli, B., Ibar, E., et al. 2010b, Astronomy and Astrophysics, 518, L31
- Jarvis, M. J., Smith, D. J. B., Bonfield, D. G., et al. 2010, Monthly Notices of the Royal Astronomical Society, Volume 409, Issue 1, pp. 92-101., 409, 92
- Jarvis, M. J., Taylor, A. R., Agudo, I., et al. 2016, Proceedings of Science, 6 Jin, S., Daddi, E., Liu, D., et al. 2018, The Astrophysical Journal, 864, 56
- Kartaltepe, J. S., Mozena, M., Kocevski, D., et al. 2015, Astrophysical Journal, Supplement Series, 221, 11
- Kashino, D., Silverman, J. D., Sanders, D., et al. 2019, The Astrophysical Journal Supplement Series, 241, 10
- Kennicutt, R. C. 2003, https://doi.org/10.1146/annurev.astro.36.1.189, 36, 189
 Khostovan, A. A., Kartaltepe, J. S., Salvato, M., et al. 2025, arXiv, 18, arXiv:2503.00120
- Liu, D., Schinnerer, E., Groves, B., et al. 2019, ApJ
- Madau, P. & Dickinson, M. 2014, Annual Review of Astronomy and Astrophysics, 52, 415
- Magnelli, B., Ivison, R. J., Lutz, D., et al. 2015, Astronomy and Astrophysics, 573, A45
- Maini, A., Maini, & Alessandro. 2017, PhDT
- Middelberg, E., Deller, A. T., Norris, R. P., et al. 2013, Astronomy and Astrophysics, 551, A97
- Middelberg, E., Norris, R. P., Hales, C. A., et al. 2010, A&A, 526, A8
- Molnár, D. C., Sargent, M. T., Delhaize, J., et al. 2018, Monthly Notices of the Royal Astronomical Society, 475, 827
- Molnár, D. C., Sargent, M. T., Leslie, S., et al. 2021, Monthly Notices of the Royal Astronomical Society, 504, 118
- Morabito, L. K., Kondapally, R., Best, P. N., et al. 2025, MNRAS, 536, L32
- Morabito, L. K., Sweijen, F., Radcliffe, J. F., et al. 2022, MNRAS, 515, 5758
- Njeri, A., Beswick, R. J., Radcliffe, J. F., et al. 2023, Monthly Notices of the Royal Astronomical Society, 519, 1732
- Novak, M., Smolči´c, V. S., Schinnerer, E., et al. 2018, Astrophysics A&A, 614, 47
- Ponnada, S. B., Cochrane, R. K., Hopkins, P. F., et al. 2025, The Astrophysical Journal, Volume 980, Issue 1, id.135, 15 pp., 980, 135
- Radcliffe, J. F., Barthel, P. D., Garrett, M. A., et al. 2021, Astronomy and Astrophysics, 649, L9
- Radcliffe, J. F., Beswick, R. J., Thomson, A. P., et al. 2024, MNRAS, 527, 942
 Radcliffe, J. F., Garrett, M. A., Muxlow, T. W., et al. 2018, Astronomy and Astrophysics, 619, A48
- Rampadarath, H., Morgan, J. S., Soria, R., et al. 2015, MNRAS, 452, 32
- Rickard, L. J. & Harvey, P. M. 1984, Astronomical Journal, Vol. 89, p. 1520-1530 (1984), 89, 1520
- Rivera, G. C., Williams, W. L., Hardcastle, M. J., et al. 2017, Monthly Notices of the Royal Astronomical Society, 469, 3468
- Sarbadhicary, S. K., Tremou, E., Stewart, A. J., et al. 2021, The Astrophysical Journal, 923, 31
- Sargent, M. T., Schinnerer, E., Murphy, E., et al. 2010, The Astrophysical Journal Supplement Series, 186, 341
- Schinnerer, E., Weiss, A., Aalto, S., & Scoville, N. Z. 2010, ApJ, 719, 1588
- Schober, J., Sargent, M. T., Klessen, R. S., & Schleicher, D. R. 2023, Astronomy & Astrophysics, Volume 679, id.A47, <NUMPAGES>20</NUMPAGES> pp., 679, A47
- Scoville, N., Abraham, R. G., Aussel, H., et al. 2007, The Astrophysical Journal Supplement Series, 172, 38
- Shuntov, M., Ilbert, O., Toft, S., et al. 2025, A&A, 695, A20
- Smith, D. J., Haskell, P., Gürkan, G., et al. 2021, Astronomy and Astrophysics, 648, A6
- Ulvestad, J. S., Antonucci, R. R. J., & Barvainis, R. 2004, The Astrophysical Journal, Volume 621, Issue 1, pp. 123-129., 621, 123
- V., S., Baran, N., Novak, M., et al. 2017, A&A, 602
- van der Wel, A., Bezanson, R., D'Eugenio, F., et al. 2021, The Astrophysical Journal Supplement Series, 256, 44
- Wang, T. M., Magnelli, B., Schinnerer, E., et al. 2022, Astronomy and Astrophysics, 660, A142
- Whittam, I. H., Jarvis, M. J., Green, D. A., Heywood, I., & Riley, J. M. 2017, Monthly Notices of the Royal Astronomical Society, 471, 908
- Yang, L., Kartaltepe, J. S., Franco, M., et al. 2025, Ghassem Gozaliasl, 8, 20 Yoon, I. 2024, The Astrophysical Journal, 975, 15

Appendix A: Evolution of q_{IR} with redshift

In Figure A.1 we show that q_{IR} evolves with the redshift following a power law $(1 + z)^A$ (e.g. black line). This is because our targets were drawn from a flux-limited sample of joint IR and radio detections. From a non-linear squares (NLS) method, we find $A = -0.19 \pm 0.03$, in agreement with e.g. Delhaize et al. (2017). The same figure shows that our 4 VLBA detections (blue stars) are placed at different redshifts. The statistic is too low to explore the observed q_{IR} distribution in multiple redshift bins, and for this reason, we decided to re-scale the q_{IR} values to the same redshift, choosing a reference value z_0 . We compute the z-corrected q_{IR} using the expression:

$$q_{IR,z_0} = q_{IR}(z) \left(\frac{1+z_0}{1+z}\right)^A \tag{A.1}$$

where z_0 is the reference redshift, that we set to an arbitrary value of $z_0 = 0.5$. Finally, we show the 42 SFG (green dots in Fig. A.1) of the (M_{\star}, rms) - CS, by considering those VLBA observations in regions deep as or deeper than 6.7 μ Jy beam⁻¹ (i.e., the poorest sensitivity reached among the detections). We find that the distributions of the mass-matched CS and the mass- and rms-matched CS spread randomly around the IRRC, indicating that systematic effects are absent.

Then, we compute the corrected q_{IR,z_0} ($q_{IR,z_0,corr}$) of the 4 detections by subtracting the VLBA fluxes arising from the AGN, which is $\log(L_{1.4GHz,VLA}[W/Hz] - L_{1.4GHz,VLBA})$. Figure A.2 shows the distribution of the $q_{IR,z_0,corr}$ of the 4 detections (blue histogram) and the q_{IR,z_0} of the control sample (yellow histogram). The bin size is 0.2 dex, that is about twice larger than the average q_{IR} uncertainty.

The red curve is the Gaussian fit of the real distribution. The gray curve is obtained by extracting 1000 values from the so-called "mirror distribution" (hatched histogram) using a bootstrap method, which would represent the distribution observed if all galaxies were star-forming. The errors used in the bootstrap are the $16^{th}/84^{th}$ percentiles of the 1000 values. The mirror distribution is obtained by unfolding the right-hand side of the distribution (above the peak, which is assumed to originate from pure SF) on the left side. A K-S test was not able to exclude that the mirror and the real distribution are drawn from different parent samples (with a p-value of 0.99). Accordingly, the median value of the real distribution, which is $\mu_R = 2.67^{+0.02}_{-0.02}$, and the median of the bootstrapped-mirror distribution ($\mu_{\overline{M}}$ = $2.69_{-0.04}^{0.04}$), are consistent between the errors on the medians, computed as the $16^{th}/84^{th}$ percentiles of the respective distributions divided by the root squared number of the total counts. Thus, as expected, the real distribution matches the mirrored

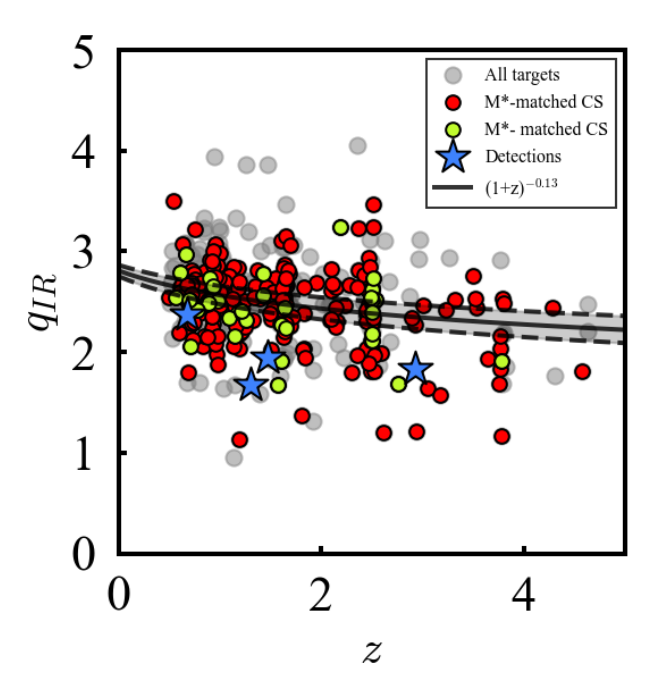


Fig. A.1. q_{IR} as a function of redshift for all the 500 targets (grey points), the 4 VLBA-detected AGN (dark blue stars) and the 277 non-detections that constitute the M_{\star} -matched sample (red points). The green dots are the 42 non-detections which make the (M_{\star}, rms) -matched control sample. The black line is the NLS fit of all the targets described by the power law $(1+z)^{-0.13}$.

one after subtracting the AGN contribution from the q_{IR,z_0} . To explore the effects of the correction from the AGN

To explore the effects of the correction from the AGN contribution, we study q_{IR,z_0} in two different scenarios: (1) without the VLBA correction for both detections and non-detections; and (2) only for the control sample of non-detections. Interestingly, the real and mirrored distributions are still statistically indistinguishable in the (1) case. The bottom panel of Figure A.2, indeed, shows that $\mu_R = 2.65^{+0.02}_{-0.01}$ and $\mu_{\overline{M}} = 2.69^{+0.04}_{-0.04}$, which are (again) consistent within the error bars between each other and with the values in Fig. A.2. However, the difference between μ_R and μ_M is ~ 0.04 dex and larger than when considering the AGN-corrected q_{IR,z_0} . We also observe a slight shift on the left side between the red and black curves, reflecting the fact that all the detections have $q_{IR,z_0} < \mu_R$. The shift, indeed, disappears in the central panel of Fig. A.2 when we consider SFG-only from the control sample. Finally, the values of μ_R are identical among the (1) and (2) cases. In conclusion, we can robustly claim that VLBA AGN contamination, despite being non-negligible for individual detections, does not impact at all the peak position (and the overall shape) of the original q_{IR} distribution.

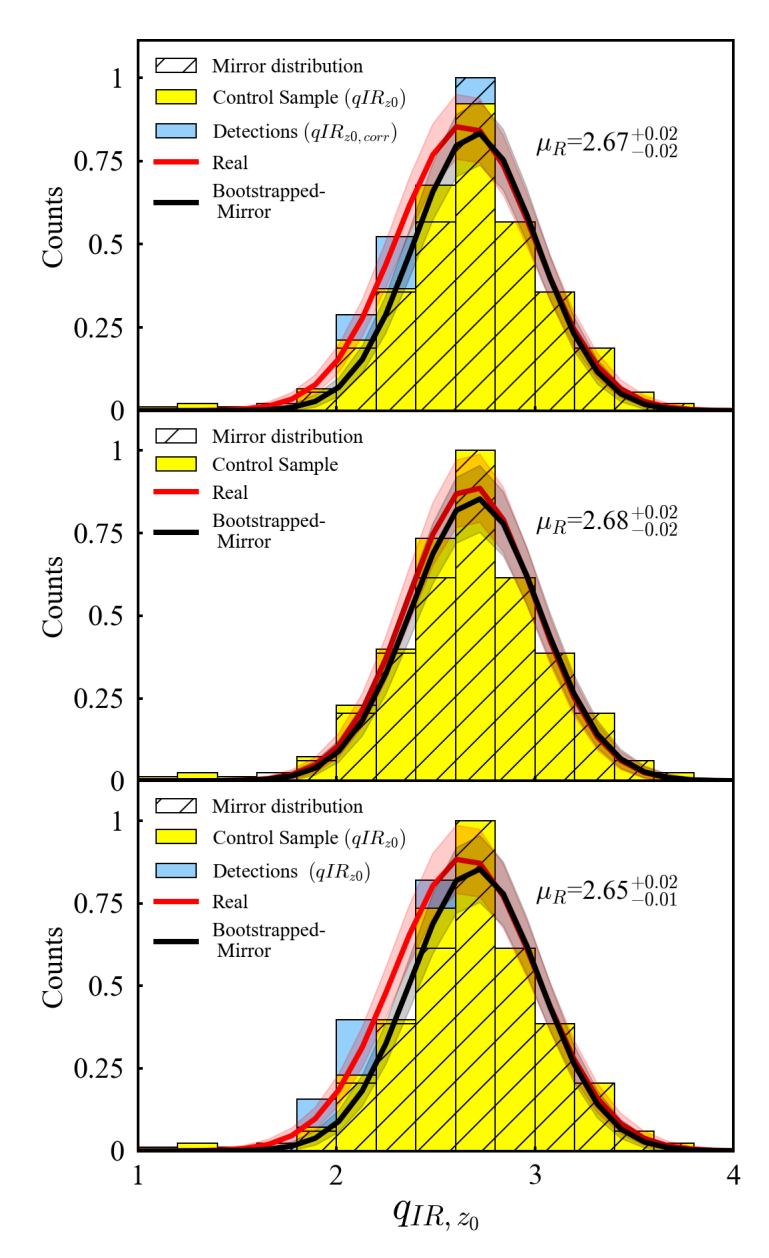


Fig. A.2. Normalized q_{IR} distributions re-scaled to $z_0 = 0.5$ (q_{IR,z_0}) for the control sample of VLBA non-detections (yellow histogram), while the 4 detections (light blue histogram) are shown both before (bottom panel) and after the VLBA AGN correction (top panel). The red Gaussian is the fit of the yellow+blue (or yellow) histograms, while the black curve is the Gaussian fit to the bootstrapped mirror distribution.